Activated carbon with exceptionally high surface area and tailored nanoporosity obtained from natural anthracite and its use in supercapacitors

Ouassim Boujibar, Fouad Ghamouss, Arunabh Ghosh, Ouafae Achak, Tarik Chafik

Activated carbon with exceptionally high surface area and tailored nanoporosity obtained from natural anthracite and its use in supercapacitors

Ouassim Boujibar[a,b], Fouad Ghamouss[b,*], Arunabh Ghosh[b], Ouafae Achak[a] and Tarik Chafik[a,*]

[a]Laboratory LGCVR-UAE/U14FST, Faculty of Sciences and Techniques, University Abdelmalek Essaadi, Tangier, Morocco.

[b]PCM2E, EA 6299 Université François Rabelais de Tours, Parc de Grandmont, 37200 Tours, France.

*Corresponding author.

E-mail address: fouad.ghamouss@univ-tours.fr (F. Ghamouss). t.chafik@fstt.ac.ma (T. Chafik).

Abstract

We have developed high performance supercapacitor electrodes while demonstrating that using one-step simple industry friendly activation technique, precise control over pore size distribution can be obtained from natural resource. Irrespective of the same staring material, natural anthracite, the obtained samples exhibited two distinctly different pore size distributions exploiting the size differences of the activating agents, which are potassium (KOH) and sodium (NaOH) ions respectively. This precise control over pore sizes enabled us to obtain an unprecedented observation of 136% enhancement of energy density while there is no loss of power density was observed. This unique observation is a result of almost no loss in ion diffusion properties within the electrodes, irrespective of the change of electrolyte to more viscous ionic liquid (Ethyl-Methyl Imidazolium Tetrafluoroborate) from a less viscous aqueous and organic based electrolytes. This size-selective activation enabled us tailoring a highly desirable pore size distribution, a combination of bigger micropores and smaller mesopores. This not only provided very high specific surface area of 2934.60 m^2/g with a total pore volume of 1.33 cm^3/g, and highest capacitance (198.15 F/g) in aqueous electrolyte, it has also resulted in very high energy density of 82.93 Wh/kg and high power density of ~3487 W/kg.

Keywords:

Supercapacitor; ionic liquids; activated carbon; natural anthracite;

1. Introduction

The ever-increasing demand for energy has led the researchers around the world to develop advanced energy storage systems. This issue redirected a lot of focused research efforts on the performance improvements of different type of energy storage devices, such as lithium or sodium ion batteries, fuel cells, and the supercapacitors. Among these, supercapacitors are considered the strongest contenders for high-power applications [1–4]. Electrical double-layer capacitors (EDLCs) are the type of supercapacitors which store energy by pure electrostatic process with no chemical reaction or charge transfer (Faradaic) involved, which has established EDLCs as most electrochemically stable type of supercapacitors with thousands of cyclic stability. Also, pure electrostatic interactions are much faster than faradaic processes, which enables EDLCs having high-power density, and hence EDLCs hold strong promise for energy storage applications [5]. The aforementioned advantages strongly depend on the electrode materials of carbon-based supercapacitors that requires a high specific surface area accessible to ions and a suitable pore size distribution [6]. A remarkable number of different type of porous carbon materials with large surface area, such as graphene, carbon nanotubes, carbon nanofibers and almost all type of activated carbon sources have been investigated to check their performances as electrodes for EDLCs applications [7–9]. To date, activated carbons have been the material of choice for the supercapacitor electrode fabrication mainly due to their low cost, high specific surface area and excellent stability [10].

The majority of available activated carbon materials are prepared by physical and/or chemical activation of various carbon-rich precursors [11]. In physical activation, the precursors are first carbonized, then followed by an activation step with steam or carbon dioxide [12]. In chemical activation, the precursors are impregnated with an chemical reagent and followed by a heating process under an inert atmosphere [13]. Several researches showed that KOH or NaOH-activation method as the most common manufactory route to produce micropore-rich, high pore volume, and large surface area activated carbon [14–18].

Besides, the nature of materials used as precursor is considered a key parameter governing the production of high quality activated carbons lies on the possibility of obtaining functional materials in the different application. More recently, activated

carbons from different anthracite have been used in supercapacitor applications yielding different energy density values in different electrolytes [19–23]. Nevertheless, most of them exhibit low energy density because of their low specific surface areas and/or inappropriate pore structure. While low surface area reduces over all capacitance regardless of the choice of the electrolytes, on the other hand lack of suitable porosity limits use of different non-aqueous electrolytes such as ionic liquids, electrolytes with organic solvents. These non-aqueous electrolytes generally possess much higher viscosity, especially ionic liquids are of the most viscous in nature having the difficulty to diffuse through small pores, and hence limits pore accessibility which in turn decreases capacitance. Whereas organic solvents are less viscous in nature and hence easier diffusion compared to the ionic liquids, but this advantage in ionic transport comes at the cost of compromise in the operating potential windows. This is not desirable as higher operating voltage of a capacitor and leads to significant enhancement of energy, since the energy density increases with the square of the operating voltage. Even though ionic liquids have disadvantages in terms of ionic mobility, they can provide stable operating potentials more than 3.5 V and hence much higher energy densities [24,25]. Moreover, most of the organic solvents are limited to potential windows under 2.7 V [26] and aqueous electrolytes are limited to even lower potential window up to 1.2 V, which is the water decomposition potential [27]. Ionic liquids offer greatly enhanced operation safety at high temperatures applications (≥60°C) [28,29].

Therefore, fabrication of electrodes with pore size distributions suitable for ionic liquids is of great importance, which demands precise control over pore creations within a porous electrode. Also, pore sizes are of utmost importance when we consider anions and cations of different sizes, as pore size plays a decisive with respect to adsorption within a pore and hence directly controls the amount of charge storage within the system [30].

When we consider different porosity, we know that ultra-micropores maximize surface area but they suffer from slow ion diffusion speed, whereas bigger mesopores provide very fast ion transport, but they suffer from poor material density and overall low total surface area. Therefore, a combination of bigger micropores and smaller mesopores are the key to obtain optimum energy density and power density [31]. However, achieving this pore combination is not straightforward, and therefore highly microporous conventional activated carbon deliver unsatisfactory performance with highly viscous

and low diffusivity ionic liquids in the porosity curtailing the performance of supercapacitor device [32]. Pore size distribution of an activated carbon depends upon many parameters, such as activating agents, the nature of starting material and obviously on the activation process.

Therefore, in this work we have carefully chosen a Moroccan anthracite, which is of high crystallinity and of high purity, to get rid of unwanted defects which results in uncontrolled porosity, which may not be appropriate for the ionic liquid in concern. Hence, unwanted pores would increase the amount of dead volume of the material contributes to reduction of the material density which in turn compromises volumetric capacitance, mechanical strength and over all conductivity of the electrode materials.

For these reasons an empirical approach was adopted for the investigation of the experimental conditions of activated carbon preparation using two different activating agents containing two different elements K and Na of different sizes so as to assess the conditions permitting better control over the sizes of the created pores. The as prepared activated carbons samples were tested as supercapacitor electrodes using three different electrolytes, which are 0.5M K_2SO_4 (aqueous electrolyte), 1M Et_4NBF_4/ACN (organic-solvent) and $EmimBF_4$ (ionic liquid). The obtained results have been discussed and compared with respect to other cutting-edge research results.

2. Material and methods

2.1. Chemical activation of the raw anthracite

The raw anthracite (ANT-raw) collected from oriental region of Morocco (Jerrada), was used as the precursor for production the activated carbons electrode supercapacitors. Firstly, the dried raw anthracite was washed with distilled water and dried in an oven at 100°C for 24 hours, then crushed and sieved to retain the fraction between 500 and 1000 µm. A chemical activation method was employed to prepare activated carbon. ANT-raw powder was first crushed and sieved, and then chemically activated using potassium hydroxide (KOH) or sodium hydroxide (NaOH) as an activating agent. The mass ratio of powdered ANT-raw to the activation agent 1/4 were taken, a 16 g of KOH or NaOH lentils were directly mixed with a given amount of 4g of ANT-raw at room temperature. This process was done in absence of water. After mixing, the resulting samples were heat-treated under N_2 flow of 600 cm^3/min at a 850°C for 1 hour with a heating rate of 5 °C /min. Subsequently, the blended samples were allowed to cool

down to the room temperature under nitrogen flow. Finally, all the as-obtained activated carbons were washed with HCl (5M) solution, then with deionized water again until reaching pH value of the rinse reaches around 7. Such washing steps were required for eliminating metallic potassium or sodium, any possible presence of excesses hydroxides and soluble impurities in the char. The resultant material powder was dried for 24 h inside an oven. The activated carbons prepared from ANT-raw were named as ANT-K-ACT and ANT-Na-ACT, according to the activating agent utilized K for KOH and Na for NaOH, respectively.

2.2. Characterization of the activated carbons

The activation temperature of the Moroccan raw anthracite was decided based on the thermo-gravimetric and differential scanning calorimetry analysis using SDT Q600 TA Instruments under a nitrogen flow. The activated carbon samples were comprehensively characterized in order to determine the structural and textural properties. The sample morphology was investigated by scanning electron microscopy (SEM, Model SH-4000M) at an acceleration voltage of 15 kV. The crystalline structure was examined by X-ray diffraction (XRD) analysis using Brukereco D8 Advance diffractometer. Raman spectroscopy (LabRAM HR Raman spectrometer) study was carried out to understand the crystallinity of graphitic planes and disordered region of the prepared activated carbons. The porous characteristics were analyzed using N_2 adsorption isotherms measured at 77 K using Micromeritics ASAP 2020 apparatus for relative pressure values (P/P_0) ranging between 10-8 and 0.90. The specific surface area was obtained according to the Brunauer-Emmett-Teller theory (S_{BET}) [33], considering the molecular cross-sectional area of N_2 at 77 K to be 0.162 nm^2. Before analysis, the all samples were degassed during 4 hours at 523 K. The total pore volume (V_T) was obtained from the N2 adsorption at P/P_o= 0.90. Thus, the micropore volumes (V_{HK}) were determined by the Horvath–Kawazoe equation [34] for samples based on the N_2 isotherm adsorption data. Mesopores volume, V_{meso}, was calculated from the difference between V_T and V_{HK} [35]. The density functional theory (DFT) method assuming a slit pore geometry was applied to obtain the pore size and energy distribution [36].

2.3. Electrochemical measurements

The electrochemical characterization of as-prepared materials were studied by Cyclic Voltammetry (CV), ~~and~~ Galvanostatic Charge-Discharge (GCD) and Electrochemical

Impedance Spectroscopy (EIS) using a computer controlled potentiostat (Biologic VMP3, France). The working electrodes were fabricated using a mixture containing 70 wt. % of the as prepared activated carbons, ~~7~~ 23 wt. % carbon black as a conductive agent, and ~~23~~ 7 wt. % polytetrafluoroethylene (PTFE) binder dispersed in ethanol. After pressing a rectangular carbon plate on a stainless steel mesh, it was dried in an oven at 60°C for 24 h. The electrochemical measurements were performed in a three-electrode configurations using 0.5 M K_2SO_4 as the electrolyte. The CV and the GCD experiments were carried out from the potential range of -1.0 to 0 V (vs. SCE) at various scan rates and different specific current ~~densities~~. The specific capacitance values were determined from discharge curve of the GCD using the following equation (1).

$$C_{sp} = \frac{I \times \Delta t}{m \times \Delta V} \qquad \text{Eq (1)}$$

Where C_{sp} (F/g) is the specific capacitance of the material, I (A), t (s) and m (g) are the discharge current, discharge time, and the effective mass loaded on a single working electrode, respectively. V (V) refers to the potential change excluding the voltage drop within a given time t. In order to study the potential of the materials from a practical application point of views, the electrode materials were studied in two-electrode configuration as well using both organic and ionic liquid electrolytes. Symmetrical electrochemical capacitors were built using two carbon electrodes of similar mass and electrically isolated by glassy fibrous separator (Whatman, 50 µm). The organic-solvent and the ionic liquid electrolytes was 1M tetraethylammonium tetrafluoroborate in acetonitrile (Et_4NBF_4/ACN) and 1-ethyl-3-methyl imidazolium tetrafluoroborate ($EmimBF_4$), respectively. From the GCD, the total specific capacitance C_t (F/g) in a symmetrical system was determined using equation (1) replacing (m) by the mass of the two electrodes. The values of the specific energy E (Wh/kg) and specific power P (W/kg) were calculated using equations below, respectively [37]:

$$E = \frac{1}{2} \times C_t \times (\Delta V)^2 \qquad \text{Eq (2)}$$

$$P = \frac{E}{\Delta t} \qquad \text{Eq (3)}$$

3. Results and discussion

3.1. Textural and structural properties of the activated carbons

Fig. S1 (***Supporting Information***) shows both the thermal gravimetric analysis (TGA) and differential scanning calorimetry (DSC) profiles, obtained from Moroccan raw

anthracite. A remarkable thermal stability was observed for the studied anthracite due to its graphitic structure. When this raw coal was heated up to 900°C under nitrogen, a very little weight loss of only about 12% was observed. The first weight loss of 5 % and an endothermic peak, were observed within temperatures ranging from 40 °C to 190 °C, which are attributed to the released of volatile matters and moistures [38]. This indicates that content of the volatile matter is low, confirming good quality of the coal. The second decomposition stage of the profile showing a weight loss of 7% within a temperature range, from 500 °C to 700 °C, due to the depolymerization of the ANT-raw macromolecular network by cleaving weak covalent bonds [39,40].

Elemental analysis results are presented in **Table 1**, approved the high carbon content of the Moroccan raw anthracite (87 wt. %) and the low volatile matter content, in agreement with our TGA analysis (**Fig. S1**, ***Supporting Information***). These result indicated the high purity of the studied anthracite according to the coal characteristics classification guideline following International Organization for Standardization; ISO 11760:2018 [41]. This finding suggests the advantage of using this anthracite as precursor for activated carbon. Note that during activation process, the oxygen content increased considerably while carbon content decreased. This could be due to surface oxidation by KOH and NaOH during the activation. This means that carbon release is, apparently, driven by the formation of oxygen functional groups leading to formation of CO and CO_2 as reported by M.A. Lillo-Ródenas et al [42]. Additionally, it is interesting to note that the percentage of the sulphur in the activated carbon product is decreased from 0.86 wt. % for the ANT-raw sample to 0.27 wt. % for the ANT-K-ACT and removed for the ANT-Na-ACT.

Table 1 Elemental analysis of the ANT-raw and the prepared active carbons.

Sample	Elements (wt.%)				
	Carbon	Hydrogen	Nitrogen	Oxygen	Sulphur
ANT-raw	87.32	2.39	0.98	7.46	0.86
ANT-K-ACT	73.05	1.70	0.32	17.35	0.27
ANT-Na-ACT	68.03	1.23	0.30	25.30	0.00

The surface morphology of ANT-raw and as-prepared activated carbons was observed by SEM as shown in **Fig. S2** (***Supporting Information***), where ANT-raw exhibits a compact and dense surface (**Fig. S2a**). Whereas, after activation the SEM images of ANT-K-ACT and ANT-Na-ACT samples (**Fig. S2b** and **d**, respectively), show irregular and heterogeneous surface morphology displaying pores with different sizes and shapes.

X-ray diffraction and Raman spectroscopy were used for further investigation of the crystallographic structure of the ANT-raw and the as-prepared activated carbons. As shown in, **Fig. 1a**, the ANT-raw present two broadened diffraction reflections, which were centered at around $2\theta=25.6°$ and 43.5°, respectively. The two reflections are analogous to the (002) and (100) planes of graphite, showing their dominant features of amorphous carbon [43]. After activation, the peaks of (002) and (100) have been markedly broadened and their intensities decreased dramatically for all the samples, indicating reduced crystallinity and a lower degree of graphitization in the as-obtained activated carbons, resulting in defect generation and hence pore creations due to the activation by KOH and NaOH during the chemical etching process. The Raman spectra in **Fig. 1b** of the all the as-prepared activated carbons and the ANT-raw exhibit two notable peak positions at 1330 cm^{-1} and 1598 cm^{-1}, corresponding to the D (vibration of disordered sp^3 carbon) and G bands (ordered sp^2 carbon) respectively [44]. Raman spectra revealed increased value of I_D/I_G intensity ratio for the activated carbon samples compared to that of ANT-raw sample. This also confirms the reduced crystallinity of the structure within the ANT-raw samples [45], which is in good agreement with the XRD results. As reported previously, numerous defects on the carbon layers can alter the surface morphology, contributing thus to increase the total surface area and hence EDLCs. Therefore, as-prepared activated carbons with higher defect densities are expected to exhibit higher capacitance [46]. These defect densities are expected to be highly dependent on the nature activating agents used (as we discussed earlier) and we expect to obtain a tailored porosity thanks to this controlled pore creations by using two different agents (KOH and NaOH).

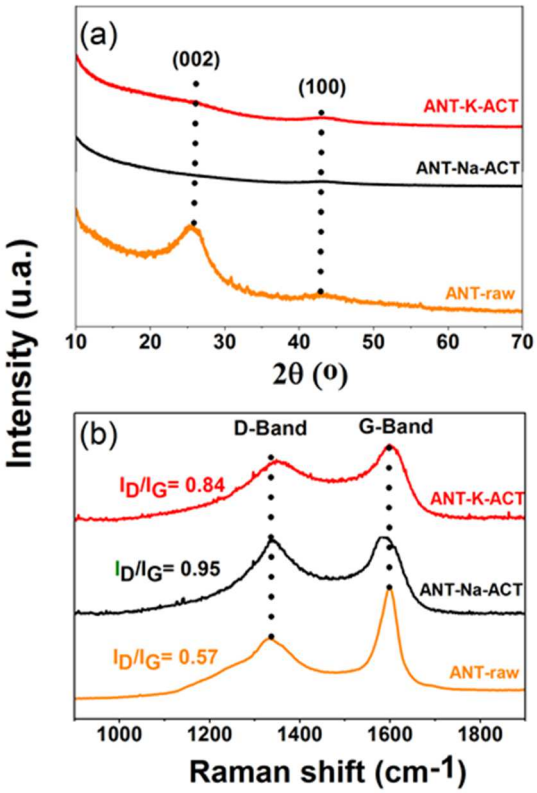

Fig. 1 (a) X-ray diffraction patterns and (b) Raman spectra of the prepared active carbons and the ANT-raw.

The porous structures of the activated samples were investigated by N_2 adsorption isotherms. As expected, the obtained results very much follow the pore size distributions profiles as presented in the **Fig 2**. Notably, all the obtained isotherms are characteristic of type I, showing similar adsorption behavior at the low relative pressure range ($P/P^o < 0.05$), confirming the presence of abundant micropores (pore width < 2 nm) for the studied samples [47].

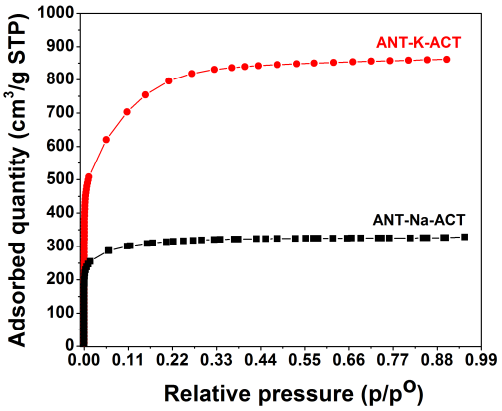

Fig. 2 Nitrogen adsorption isotherms measured at 77K for the prepared activated carbons.

The isotherms allow extraction of values the BET surface area; S_{BET}, the micropore volume; V_{HK}, the total pore volume; V_T, and the microspore's contribution to the total pore volume; V_{HK}/V_T ratio, as summarized in the **Table 2**. From the table, we can see that the ANT-K-ACT sample produced by physical mixed KOH showed the highest S_{BET} and V_T up at 2934.60 m^2/g and 1.33 cm^3/g, respectively. However, the activation by NaOH produced smaller surface areas and lower pore volumes compared to that of by KOH (**Table 2**). The V_{HK}/V_T ratio confirms that the two samples are essentially microporous, the micropore volume constituting more than 87% of the total pore volume for ANT-K-ACT, also achieved 94% for the ANT-Na-ACT.

Table 2

Sample	Surface area (m^2/g)		Pore volume (cm^3/g)			
	S_{BET}	S^a_{mic}	V^b_{Total}	V_{HK}	V_{mes}	V_{HK}/V_T (%)
ANT-K-ACT	2934.60	2110.19	1.33	1.16	0.17	87.21
ANT-Na-ACT	1199.62	1096.85	0.50	0.47	0.03	94.00

[a] Calculated from the DFT equation applied to the N_2 adsorption isotherms.
[b] Determined at $P/P_O = 0.90$ in the N_2 adsorption isotherms.

Fig. 3 shows the pore size and surface energy distributions calculated by the Density Functional Theory (DFT) method. the ANT-K-ACT exhibits a much desirable pore size distribution (**Fig. 3a**), ~~a~~ with a narrow peak centered at pore diameter width of 7.5 Å and the other one is a wider peak with its broad shoulder around 21.5 Å, and a tail spread over smaller mesoporous (~20 - 36 Å) region in between these two dominant peaks, the sample shows a considerable amount of large micropores (10 – 20 Å), and this combination is considered as very favorable pore size distribution for supercapacitor application. On the contrary, the ANT-Na-ACT sample exhibited a distinct peak only at 9 Å, and an extended tail of lower magnitude in the bigger micropore to smaller mesopore regions, as shown in the **Fig. 3a**, As a result, as we can observe from the **Table 2**, that KOH activated samples have a total specific mesoporous pore volume of 0.17 cm^3/g, compared to that of only 0.03 cm^3/g from the NaOH activated samples.

These favorable relatively larger pores obtained with KOH activated samples can be attributed to the larger radius ~~radii~~ of the K ion (220 pm), compared to that of the Na ions (180 pm). Larger K ions are expected to cause more widening of the interlayers

during activation. Thus, the creation of microporosity in carbon materials via chemical activation is partly attributed to partial gasification and expansion of the interlayer spacing's between graphitic planes through consecutive intercalation and deintercalation of K or Na [48]. As result, KOH activated samples present not only favorable pore sizes, but much higher total surface area (2934 m^2/g) in comparison with NaOH activated samples (1199 m^2/g), as indicated in the **Table 2**.

On the other hand, it's well known that the adsorption isotherms of the porous materials are strongly dependent on the structural heterogeneity of the adsorbent's surface sites and their surface energy distribution. The measured isotherms allow further determination of surface energy distribution of the activated carbon samples, calculated using the DFT equation. As shown in **Fig. 3b**, a wide distribution of the surface energy has been obtained, suggesting existence of the different type of adsorption sites, associated with different types of accessible pores (i.e. ultramicropore, micropore and mesopore) [49,50].

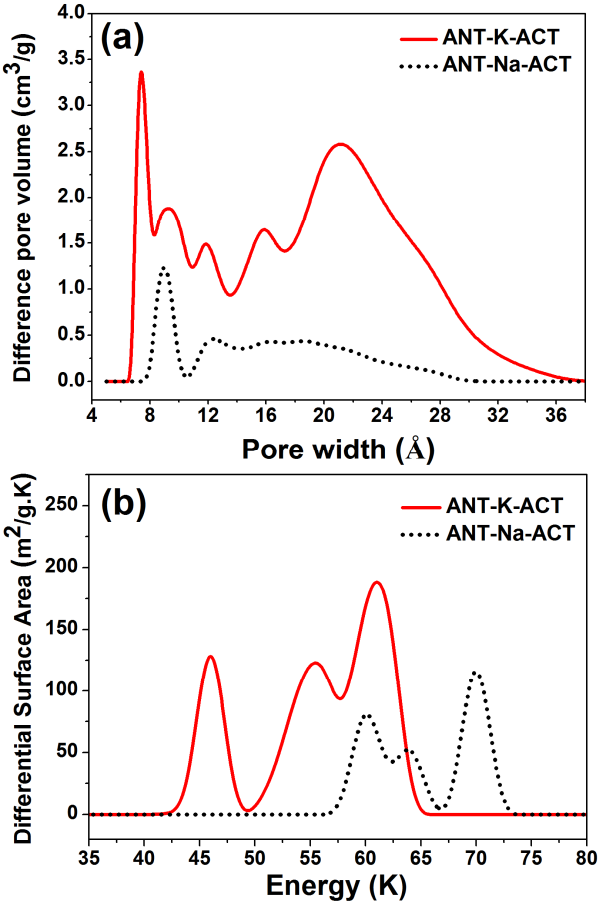

Fig. 3 (a) Pore size distribution and (b) surface energy distribution determined for the prepared active carbons using DFT calculations applying in N_2 adsorption isotherms.

2.1. Electrochemical measurement

At first, the electrochemical performance of the as-prepared materials was evaluated ~~were evaluated~~ by a three-electrode system in 0.5 M K_2SO_4 electrolyte. **Fig. 4a** displays CV curves of all the samples at a scan rate of 2 mV/s in a voltage window from −1 to 0V versus SCE. The CV curve of the ANT-raw sample exhibited a triangle-shaped current-voltage (I-V) profile with low area between the charge-discharge curves of the CV, indicating poor charge storage capacitance. After chemical activation, all the samples exhibited approximately rectangular shape, suggesting enhanced capacitive behavior. Notably, the CV curves do not show any distinct peak, which indicates the absence of strong pseudocapacitive phenomena, thanks to the high purity of the anthracite samples. The ANT-K-ACT exhibited the largest area for the CV loops among all the samples, implying its excellent charge storage properties. CV curves of the ANT-K-ACT and ANT-Na-ACT electrodes at different scan rates from 2 mVs^{-1} to 50 mVs^{-1} are displayed in Fig. 4b and c, respectively. From the CV results, it can be clearly found that the electrode materials obtained similar rectangular shapes at the lower scan rates, confirming that the capacitance obtained was mainly due to double-layer capacitor nature of the charge-discharge process. However, the rectangular CV curves is slightly distorted at a scanning rate of 50 mV/s, which indicates the smooth motion of electrolyte through the pores gets affected slightly because of reduced time for higher scan rate sweeps [51]. **Fig. 4**d showed the GCD plots at different specific current ~~densities~~. The charging and discharging curves exhibited linear and symmetrical shapes at the tested specific current ~~densities~~, suggesting they possess excellent electrochemical reversibility, which is highly desirable for EDLCs. In addition, no obvious potential drop is observed from the GCD curves, further confirming the good electrical conductivity of the electrodes. According to the **Eq (1)**, the specific capacitance of the samples plotted against the specific current ~~density~~ in **Fig. 4e**, decreased for both the samples with increased specific current ~~density~~ because of the obvious diffusion limitations of electrolyte ions within the pores of the material. It can be clearly observed that the capacitive performance, both in terms of the specific capacitance and rate

performance, showing better performances for ANT-K-ACT sample than others. The highest specific capacitance values of up to 198.15 F/g and 135.19 F/g at 0.1 A/g and 2 A/g specific current ~~densities~~ respectively, thanks to the higher specific surface area of ANT-K-ACT sample as indicated in **Table 2**.

To better investigate the resistance of the electrodes, EIS test was used to characterize the impedance and ion diffusion process of ANT-K-ACT and ANT-Na-ACT electrodes. Fig. 4f shows the Nyquist impedance spectra obtained in 0.5 M K_2SO_4 electrolyte at a frequency range from 5mHz to 500kHz. As expected, both electrodes showed a typical behavior of capacitive and porous interfaces i.e. at high frequencies, a depressed semi-circle, followed by an inclined line in the mid-region of the frequencies (Warburg region) and a straight line which is almost parallel to the imaginary axe of the impedance at low frequencies region. Furthermore, one can notice that the ANT-K-ACT sample exhibits a small diameter for the semicircle in the moderate frequency region, smaller Warburg portion at middle frequency range (inset in Fig. 7b) and a straight-line slope close to 90º degrees at the low frequency region, demonstrating fast charge transfer and good capacitive behavior, which is again in agreement with the results obtained from CV and GCD. This is ascribed to the good textural properties of the the ANT-K-ACT, including high specific surface area and suitable porosity for the electrolyte ions. However, the predominated micropore of ANT-Na-ACT as indicated by a large fraction of Vmicro (94%) greatly impedes the ion transport due to its long and torturous channels, giving rise to a large internal resistance and poor capacitive performance.

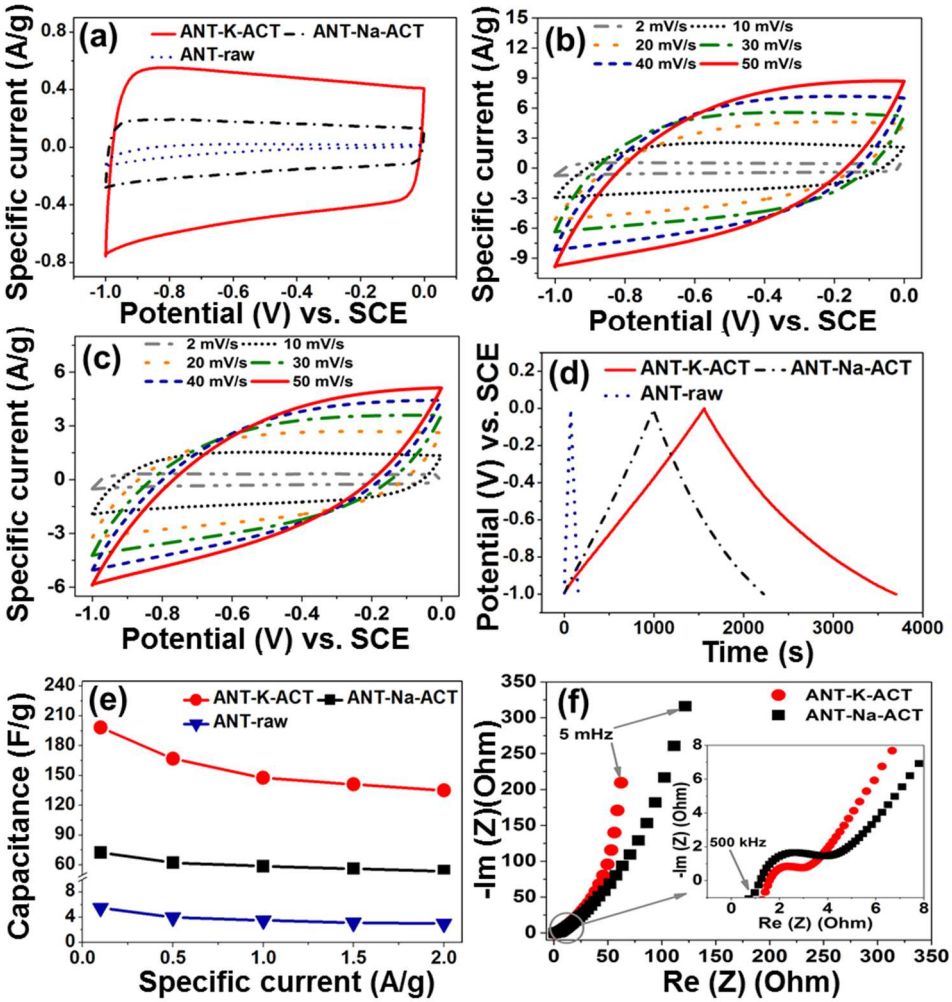

Fig. 4 Electrochemical performance of the as-prepared samples in 0.5 M K_2SO_4 electrolyte, (a) CV curves at a scan rate of 2 mV/s, (b) CV curves at various scan rates of the ANT-K-ACT, (c) CV curves at various scan rates of the ANT-Na-ACT, (d) galvanostatic charge/discharge curves at a specific current of 1 A/g, (e) specific capacitances at various specific current (0.1–2 A/g) and (f) Nyquist plots.

It should be pointed out from the practical point of view, that the aqueous electrolyte based supercapacitors is limited due to their low cell voltage cannot be raised beyond the water decomposition potential. However, evaluation of supercapacitor performances in aqueous electrolyte, only, is not sufficient enough to conclude with respect to its performances as an electrode. Not only because aqueous electrolytes are limited by their limited potential window (1.2 V), but also other electrolytes, such as organic electrolytes and ionic liquids provide more challenges in terms of ion diffusivity, as these electrolytes are more viscous in nature, and hence reduced ionic conductivity regarding their larger ion sizes compared to aqueous electrolytes.

Therefore, in order to determine the true potential of the studied electrodes, the electrochemical performance of the both ANT-K-ACT and ANT-Na-ACT samples have been investigated using a two-electrode system in two different type of electrolytes. 1M Et_4NBF_4/ACN and $EmimBF_4$ used as organic-electrolyte and ionic liquid electrolytes respectively.

In order to determine the operating voltage limit, the CV at a scan rate of 20 mV/s was carried out in different voltage ranges for a symmetric capacitor based on identical electrodes from the ANT-K-ACT and ANT-Na-ACT in the both electrolytes types. **Fig. 5** shows the CV obtained in 1M Et_4NBF_4/ACN ~~Et4NBF4/CAN~~ and $EmimBF_4$. It was found that, in an Et_4NBF_4/ACN medium, an ideal behavior with a rectangular CV shape and of not present any distinct peaks using an operating voltage of 2.5 V. Whereas the shapes of the CV curves remain rectangular up to 3.5 V for $EmimBF_4$ electrolyte, indicating the excellent electrochemical stability. Here, it is highly interesting to observe comparatively narrower shapes of CVs for the Na-activated samples (**Fig. 5b** and **d**) both in the 1M Et_4NBF_4/ACN ~~Et4NBF4/CAN~~ and $EmimBF_4$ electrolytes, whereas the CV shapes are significantly wider ~~narrower~~ for the latter case (**Fig. 5d**). This is a clear indication of better charge storage performance of the K-activated sample.

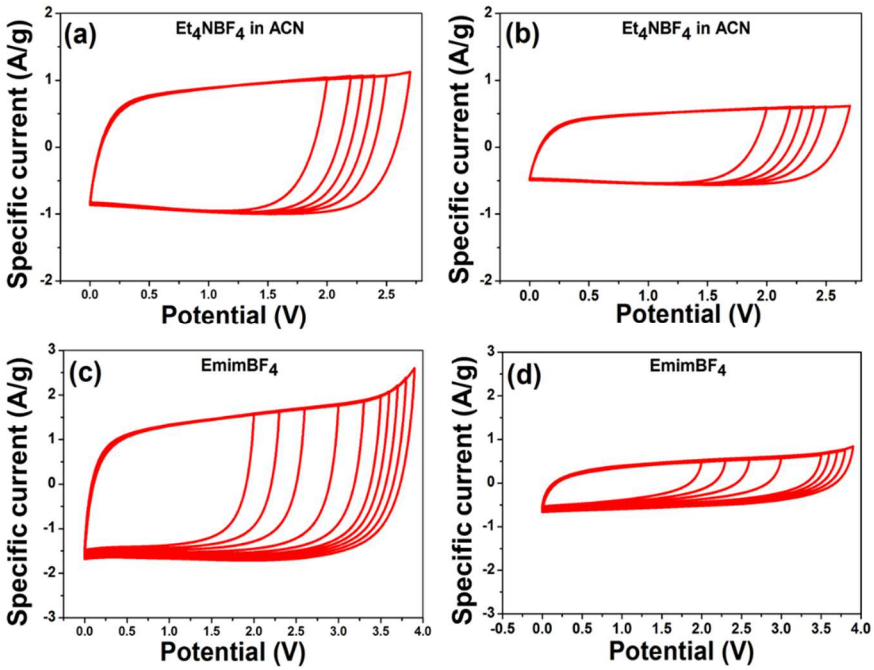

Fig. 5 CV curves at a 20 mV/s of the symmetric two-electrode cell at different voltage windows in 1M Et_4NBF_4/ACN of the ANT-K-ACT (a), ANT-Na-ACT (b) and in $EmimBF_4$ of the ANT-K-ACT (c), ANT-Na-ACT (d).

The GCD tests were performed to evaluate the specific capacitance and to assess the energy and power performance for both the ANT-K-ACT and ANT-Na-ACT samples, assembled symmetric two-electrodes configuration. **Fig. 6** shows comparative rate performances of both the ANT-K-ACT ~~ANT-Na-ACT~~ (**Fig. 6a**) and ANT-Na-ACT ~~ANT-K-ACT~~ (**Fig. 6b**) samples in both the Et_4NBF_4/ACN and $EmimBF_4$ electrolytes. Capacitance retentions, (C/C_0 in %, while C_0 is initial capacitance and C is measured capacitance at different specific current ~~densities~~), were plotted against different specific current ~~densities~~ and it's been observed that ANT-K-ACT samples shows an excellent C/C_0, more than 88%, whereas ANT-Na-ACT samples' C/C_0 drops down to a value approximately 82%. However, when we look at the performance in the ionic liquid electrolyte, we can clearly see that ANT-K-ACT samples significantly outperforms ANT-Na-ACT samples by maintaining a C/C_0 value of 72%, whereas in the latter case the C/C_0 value drops down to only 12%. This observation is very important and most significant in terms of describing the porosity of the ANT-K-ACT samples, it can be clearly observed that ~~for~~ **even for a** higher viscous medium we could obtain much faster charge transport compared to that of ANT-Na-ACT samples, thanks to the comparatively bigger pore size distribution of the ANT-K-ACT samples, as we have shown in **Fig. 3a**. Also, maintaining high C/C_0 value strongly indicates a good interconnected porosity within the sample.

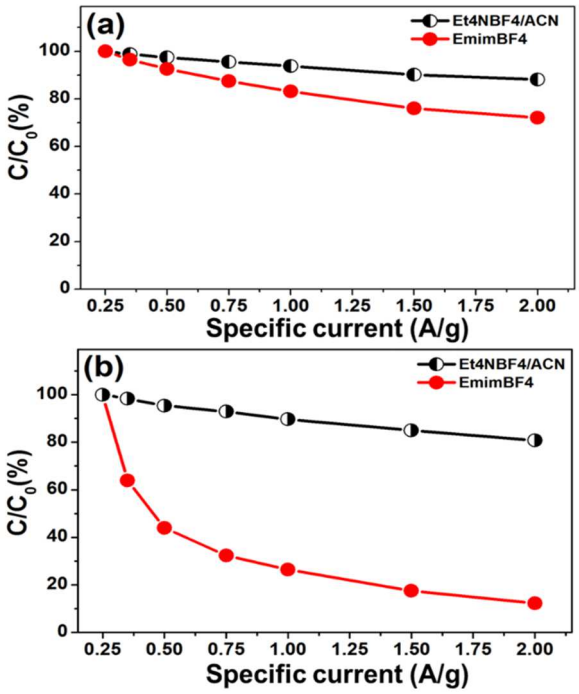

Fig. 6 Comparative rate performances of both the ANT-K-ACT (a) and ANT-Na-ACT (b) samples in both the Et_4NBF_4/ACN and $EmimBF_4$ electrolytes.

The above observed trend followed when the materials were compared in terms of specific energy ~~density~~ and specific power ~~density~~ of the supercapacitor. **Fig 7a** and **b** show ragone plots for both the ANT-K-ACT (**Fig. 7a**) and ANT-Na-ACT (**Fig. 7b**) samples in both the Et_4NBF_4/ACN and $EmimBF_4$ electrolytes. The ANT-K-ACT electrode clearly shows best electrochemical performances compared to ANT-Na-ACT samples in both type of electrolytes.

Irrespective of power values, the ANT-K-ACT-based supercapacitor in $EmimBF_4$ electrolyte exhibit higher specific energy ~~densities~~ by comparison to the Et_4NBF_4/ACN, due to the potential window being extended to 3.5 V in $EmimBF_4$ electrolyte. An unprecedented 136% enhancement of specific energy ~~density~~ was observed without any loss of specific power ~~densities~~. The highest specific energy ~~density~~ value of 82.93 Wh/kg was obtained in $EmimBF_4$ at a specific power ~~density~~ of 440.32 W/kg, and maintained an specific energy ~~density~~ of 58.11 Wh/kg at a specific power ~~density~~ of ~3487 W/kg. Both these performance values are better than that of using Et_4NBF_4/ACN ~~Et_4NBF_4/CAN~~ electrolyte for both the ANT-K-ACT and ANT-Na-ACT (**Fig 7b**) based supercapacitors.

Whereas, it is very important to observe that the performance of ANT-Na-ACT based supercapacitor presented lower performances when tested in $EmimBF_4$ electrolyte, which is in strong agreement with the rate capability performances as shown in **Fig. 6**. Hence, KOH activated samples seems to present an appropriate porosity as compared to that of NaOH activated samples, resulting in better performance in the presence all type of electrolytes. In addition, the energy–power characteristics of ANT-K-ACT based electrodes have been compared to those of state-of-the-art porous carbon synthesized from various materials based on total mass of active material in two electrodes (**Table 3**). Accordingly, the ANT-K-ACT based electrodes revealed promising potential compared with several activated carbons, as indicated by the values of specific energy and specific power, slightly lower than other carbon-based materials such as graphene and carbon nanotube-bridged graphene 3D. ~~Accordingly and to the best of our knowledge, the ANT-K-ACT based electrodes have among the important best energy–power characteristics ever reported for activated carbon based supercapacitors. carbon-based supercapacitors.~~

The cycling stability of the ANT-K-ACT electrodes (**Fig 7c**) were performed to examine their electrochemical stability in both the Et_4NBF_4/ACN and $EmimBF_4$ electrolytes at 1 A/g specific current ~~density~~ shows there are no significant decreases in specific capacitance values after 2000 cycles.

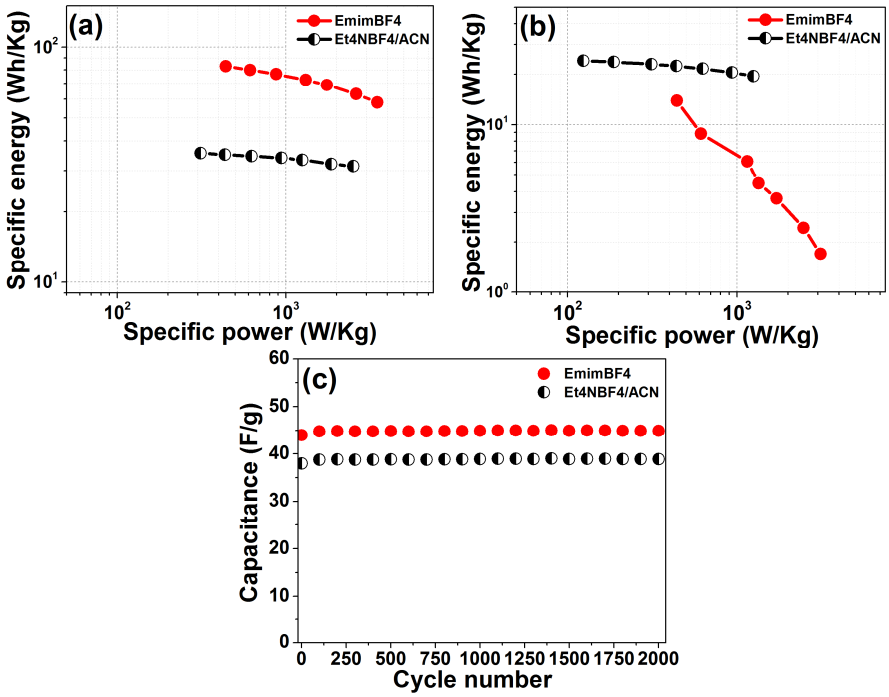

Fig. 7 Ragone plots for both the ANT-K-ACT (a) and ANT-Na-ACT (b) in both the Et_4NBF_4/ACN and $EmimBF_4$ electolytes. (c) Cycling performance plot of ANT-K-ACT symmetric supercapacitor in 1M Et_4NBF_4/ACN and $EmimBF_4$ electrolytes.

Table 3 Performance comparison of activated carbon based derived electrodes under three-electrode in aqueous electrolytes and two electrode cell system assembled with non-aqueous electrolytes.

Electrode materials	Surface area (m^2/g)	Electrolyte (voltage/V)	Capacitance (F/g)	Specific power (W/kg)	Specific energy (Wh/kg)	Reference
Moroccan anthracite	2934	$EmimBF_4$ (3.5V)	42 (1 A/g)	~1312	72.51	This work
		1M Et_4NBF_4/ACN (2.5V)	38 (1 A/g)	~1250	33.32	
		0.5M K_2SO_4	148 (1 A/g)	--	--	
Indian Cake Rusk	1413	1M $LiPF_6$ /EC:DMC (2.5V)	35 (1.75 A/g)	2234.2	31.0	[53]
		1M H_2SO_4	381 (1.7 A/g)	--	--	
Rice-straw raw	1007	$EmimBF_4$ (2.5V)	20 (0.1 A/g)	126	17.4	[54]
		1M H_2SO_4	304 (1A/g)	--	--	
Aloe vera	1890	$EmimBF_4$ (3V)	31 (0.1 A/g)	150	40	[55]
		1M H_2SO_4	347 (1A/g)	--	--	
Capsicum (bell pepper) seeds	2201	EmimTFSI (3V)	29 (0.5 A/g)	600	37	[56]
Lignin	2866	Gel PVA/LiCl	43 (0.5 A/g)	1100	55.50	[57]
Orange Peel	2160	$EmimBF_4$ (3V)	21 (1 A/g)	1185	25	[58]
Nanocellulose	1510	BMPYTFSI (3V)	16 (5 A/g)	1000	21	[59]
Raw hemp stem	2801	1.8M $TEMABF_4$/PC (2.5V)	41 (1 A/g)	21000	19.8	[60]
N-doped graphene	203	$BmimBF_4$ (3.5V)	97 (1 A/g)	1800	55	[61]
		2M KOH	390 (1A/g)	--	--	
Graphene	2400	$BmimBF_4$/ACN (3.5V)	41.5 (5.7 A/g)	250000	70	[62]
Graphene	3290	EmimTFSI/ACN (3.5V)	43.5 (4.2 A/g)	338000	74	[63]
Carbon nanotube-bridged graphene 3D	471	$BmimBF_4$ (4V)	49 (0.5A/g)	400000	110.6	[64]

4. Conclusion

We have obtained an activated carbon with high surface area with precisely controlled porosity through a simple industry friendly process, resulting in excellent supercapacitive performance with high energy density. We have obtained a highly desirable pore size distribution, which is a combination of bigger micropores and smaller mesopores, which resulted in similar ion transport irrespective of viscosity and ion sizes of the electrolytes, leading to enhancement of energy density while keeping the excellent power performance, unlike the generally observed natural trend. While exploiting the difference in K and Na ion sizes has enabled us obating two distinct and exclusive pore size distributions, at the same time thanks to the high purity of the carbon source, the obtained activated carbon materials remained free of unwanted functional groups, and provided excellent EDLC signature without noticeable pseudocapacitance. These result might paves the way for further valorization of local resources in technologically added value related to energy storage devices.

Acknowledgements

The authors would like to thank “Le Studium Loire Valley Institute for Advanced Studies” for financial support to researchers involved in this study, Pierre Ivan Raynal for his help in SEM acquisition. The CNRST/Morocco is also acknowledged for the financial support through the “project PPR2/2016/17”

References

[1] E.E. Ferg, F. Schuldt, J. Schmidt, The challenges of a Li-ion starter lighting and ignition battery: A review from cradle to grave, J. Power Sources. 423 (2019) 380–403.

[2] M. Dahbi, M. Kiso, K. Kubota, T. Horiba, T. Chafik, K. Hida, T. Matsuyama, S. Komaba, Synthesis of hard carbon from argan shells for Na-ion batteries, J. Mater. Chem. A. 5 (2017) 9917–9928.

[3] D.R. Dekel, Review of cell performance in anion exchange membrane fuel cells, J. Power Sources. 375 (2018) 158–169.

[4] Recent progress in printed flexible solid-state supercapacitors for portable and wearable energy storage, J. Power Sources. 410-411 (2019) 69–77.

[5] P. Sharma, T.S. Bhatti, A review on electrochemical double-layer capacitors, Energy Convers. Manag. 51 (2010) 2901–2912.

[6] P. Simon, Y. Gogotsi, Materials for electrochemical capacitors, Nat. Mater. 7 (2008) 845–854.

[7] Z. Yang, J. Tian, Z. Yin, C. Cui, W. Qian, F. Wei, Carbon nanotube- and graphene-based nanomaterials and applications in high-voltage supercapacitor: A review, Carbon. 141 (2019) 467–480.
[8] Z.Y. Yang, Y.H. Wang, Z. Dai, Z.W. Lu, X.Y. Gu, H. Zhao, G.Z. Sun, W. Lan, Z.X. Zhang, X.J. Pan, J.Y. Zhou, E.Q. Xie, Nature of improved double-layer capacitance by KOH activation on carbon nanotube-carbon nanofiber hierarchical hybrids for supercapacitors, Carbon. 146 (2019) 610–617.
[9] F. Tong, W. Jia, Y. Pan, J. Guo, L. Ding, J. Chen, D. Jia, A green approach to prepare hierarchical porous carbon nanofibers from coal for high-performance supercapacitors, RSC Adv. 9 (2019) 6184–6192.
[10] D.C. Martínez-Casillas, I. Mascorro-Gutiérrez, C.E. Arreola-Ramos, H.I. Villafán-Vidales, C.A. Arancibia-Bulnes, V.H. Ramos-Sánchez, A.K. Cuentas-Gallegos, A sustainable approach to produce activated carbons from pecan nutshell waste for environmentally friendly supercapacitors, Carbon. 148 (2019) 403–412.
[11] M.A. Yahya, Z. Al-Qodah, C.W.Z. Ngah, Agricultural bio-waste materials as potential sustainable precursors used for activated carbon production: A review, Renew. Sustain. Energy Rev. 46 (2015) 218–235.
[12] F. Rodríguez-Reinoso, M. Molina-Sabio, M.T. González, The use of steam and CO2 as activating agents in the preparation of activated carbons, Carbon. 33 (1995) 15–23.
[13] M. Molina-Sabio, F. Rodríguez-Reinoso, Role of chemical activation in the development of carbon porosity, Colloids Surf. Physicochem. Eng. Asp. 241 (2004) 15–25.
[14] O. Boujibar, A. Souikny, F. Ghamouss, O. Achak, M. Dahbi, T. Chafik, CO2 capture using N-containing nanoporous activated carbon obtained from argan fruit shells, J. Environ. Chem. Eng. 6 (2018) 1995–2002.
[15] D. Lozano-Castello, M.A. Lillo-Rodenas, D. Cazorla-Amoros, A. Linares-Solano, Preparation of activated carbons from Spanish anthracite: I. Activation by KOH, Carbon. 39 (2001) 741–749.
[16] J. Wang, S. Kaskel, KOH activation of carbon-based materials for energy storage, J. Mater. Chem. 22 (2012) 23710–23725.
[17] M.A. Lillo-Ródenas, D. Lozano-Castelló, D. Cazorla-Amorós, A. Linares-Solano, Preparation of activated carbons from Spanish anthracite: II. Activation by NaOH, Carbon. 39 (2001) 751–759.
[18] S. Hu, Y.-L. Hsieh, Lignin derived activated carbon particulates as an electric supercapacitor: carbonization and activation on porous structures and microstructures, RSC Adv. 7 (2017) 30459–30468.
[19] H.-C. Lee, N. Byamba-Ochir, W.-G. Shim, M.S. Balathanigaimani, H. Moon, High-performance super capacitors based on activated anthracite with controlled porosity, J. Power Sources. 275 (2015) 668–674.
[20] F. Sun, J. Gao, Y. Yang, Y. Zhu, L. Wang, X. Pi, X. Liu, Z. Qu, S. Wu, Y. Qin, One-step ammonia activation of Zhundong coal generating nitrogen-doped microporous carbon for gas adsorption and energy storage, Carbon. 109 (2016) 747–754.
[21] Z. Peng, Z. Guo, W. Chu, M. Wei, Facile synthesis of high-surface-area activated carbon from coal for supercapacitors and high CO2 sorption, RSC Adv. 6 (2016) 42019–42028.
[22] T. Guan, K. Li, J. Zhao, R. Zhao, G. Zhang, D. Zhang, J. Wang, Template-free preparation of layer-stacked hierarchical porous carbons from coal tar pitch for high performance all-solid-state supercapacitors, J. Mater. Chem. A. 5 (2017) 15869–15878.

[23] T. Pei, F. Sun, J. Gao, L. Wang, X. Pi, Z. Qie, G. Zhao, Introducing catalytic gasification into chemical activation for the conversion of natural coal into hierarchically porous carbons with broadened pore size for enhanced supercapacitive utilization, RSC Adv. 8 (2018) 37880–37889.
[24] F. Grote, Y. Lei, A complete three-dimensionally nanostructured asymmetric supercapacitor with high operating voltage window based on PPy and MnO2, Nano Energy. 10 (2014) 63–70.
[25] H. Zhong, F. Xu, Z. Li, R. Fu, D. Wu, High-energy supercapacitors based on hierarchical porous carbon with an ultrahigh ion-accessible surface area in ionic liquid electrolytes, Nanoscale. 5 (2013) 4678–4682.
[26] J.R. Miller, P. Simon, Electrochemical Capacitors for Energy Management, Science. 321 (2008) 651–652.
[27] C. Zhong, Y. Deng, W. Hu, J. Qiao, L. Zhang, J. Zhang, A review of electrolyte materials and compositions for electrochemical supercapacitors, Chem. Soc. Rev. 44 (2015) 7484–7539.
[28] A. Balducci, R. Dugas, P.L. Taberna, P. Simon, D. Plée, M. Mastragostino, S. Passerini, High temperature carbon–carbon supercapacitor using ionic liquid as electrolyte, J. Power Sources. 165 (2007) 922–927.
[29] C.-F. Liu, Y.-C. Liu, T.-Y. Yi, C.-C. Hu, Carbon materials for high-voltage supercapacitors, Carbon. 145 (2019) 529–548.
[30] B. Dyatkin, N.C. Osti, Y. Zhang, H.-W. Wang, E. Mamontov, W.T. Heller, P. Zhang, G. Rother, P.T. Cummings, D.J. Wesolowski, Y. Gogotsi, Ionic liquid structure, dynamics, and electrosorption in carbon electrodes with bimodal pores and heterogeneous surfaces, Carbon. 129 (2018) 104–118.
[31] A. Ghosh, Y.H. Lee, Carbon-Based Electrochemical Capacitors, ChemSusChem. 5 (2012) 480–499.
[32] Q.D. Nguyen, J. Patra, C.-T. Hsieh, J. Li, Q.-F. Dong, J.-K. Chang, Supercapacitive Properties of Micropore- and Mesopore-Rich Activated Carbon in Ionic-Liquid Electrolytes with Various Constituent Ions, ChemSusChem. 12 (2019) 449–456.
[33] S. Brunauer, P.H. Emmett, E. Teller, Adsorption of gases in multimolecular layers, J. Am. Chem. Soc. 60 (1938) 309–319.
[34] G. Horvath, Energetic interactions in phase and molecular level pore characterisation in nano-range, Colloids Surf. Physicochem. Eng. Asp. 141 (1998) 295–304.
[35] B. Serrano-Talavera, M.J. Muñoz-Guillena, A. Linares-Solano, C. Salinas-Martinez de Lecea, Activated carbons from Spanish coals. 3. Preoxidation effect on anthracite activation, Energy Fuels. 11 (1997) 785–791.
[36] N.A. Seaton, J.P.R.B. Walton, N. quirke, A new analysis method for the determination of the pore size distribution of porous carbons from nitrogen adsorption measurements, Carbon. 27 (1989) 853–861. doi:10.1016/0008-6223(89)90035-3.
[37] X. Tian, H. Ma, Z. Li, S. Yan, L. Ma, F. Yu, G. Wang, X. Guo, Y. Ma, C. Wong, Flute type micropores activated carbon from cotton stalk for high performance supercapacitors, J. Power Sources. 359 (2017) 88–96.
[38] B.Y. Jibril, R.S. Al-Maamari, G. Hegde, N. Al-Mandhary, O. Houache, Effects of feedstock pre-drying on carbonization of KOH-mixed bituminous coal in preparation of activated carbon, J. Anal. Appl. Pyrolysis. 80 (2007) 277–282.

[39] M. Liu, J. Yang, Y. Yang, Z. Liu, L. Shi, W. He, Q. Liu, The radical and bond cleavage behaviors of 14 coals during pyrolysis with 9,10-dihydrophenanthrene, Fuel. 182 (2016) 480–486.
[40] L. Ge, H. Feng, C. Xu, Y. Zhang, Z. Wang, Effect of hydrothermal dewatering on the pyrolysis characteristics of Chinese low-rank coals, Appl. Therm. Eng. 141 (2018) 70–78.
[41] ISO 11760:2018, Classification of coals, Int. Organ. Stand. (n.d.).
[42] M.A. Lillo-Ródenas, D. Cazorla-Amorós, A. Linares-Solano, Understanding chemical reactions between carbons and NaOH and KOH: an insight into the chemical activation mechanism, Carbon. 41 (2003) 267–275.
[43] N. Yoshizawa, K. Maruyama, Y. Yamada, E. Ishikawa, M. Kobayashi, Y. Toda, M. Shiraishi, XRD evaluation of KOH activation process and influence of coal rank, Fuel. 81 (2002) 1717–1722.
[44] A.C. Ferrari, J. Robertson, Interpretation of Raman spectra of disordered and amorphous carbon, Phys. Rev. B. 61 (2000) 14095.
[45] S. Xiong, J. Fan, Y. Wang, J. Zhu, J. Yu, Z. Hu, A facile template approach to nitrogen-doped hierarchical porous carbon nanospheres from polydopamine for high-performance supercapacitors, J. Mater. Chem. A. 5 (2017) 18242–18252.
[46] J. Vatamanu, M. Vatamanu, D. Bedrov, Non-Faradaic Energy Storage by Room Temperature Ionic Liquids in Nanoporous Electrodes, ACS Nano. 9 (2015) 5999–6017.
[47] J. Rouquerol, D. Avnir, C.W. Fairbridge, D.H. Everett, J.M. Haynes, N. Pernicone, J.D.F. Ramsay, K.S.W. Sing, K.K. Unger, Recommendations for the characterization of porous solids (Technical Report), Pure Appl. Chem. 66 (2009) 1739–1758.
[48] J. Wang, S. Kaskel, KOH activation of carbon-based materials for energy storage, J. Mater. Chem. 22 (2012) 23710.
[49] L. Dai, Carbon Nanotechnology: Recent Developments in Chemistry, Physics, Materials Science and Device Applications, Elsevier, 2006.
[50] E.A. Ustinov, D.D. Do, Application of density functional theory to analysis of energetic heterogeneity and pore size distribution of activated carbons, Langmuir. 20 (2004) 3791–3797.
[51] Y. Li, Q. Liu, W. Li, H. Meng, Y. Lu, C. Li, Synthesis and Supercapacitor Application of Alkynyl Carbon Materials Derived from CaC_2 and Polyhalogenated Hydrocarbons by Interfacial Mechanochemical Reactions, ACS Appl. Mater. Interfaces. 9 (2017) 3895–3901.
[52] P.L. Taberna, P. Simon, J.F. Fauvarque, Electrochemical Characteristics and Impedance Spectroscopy Studies of Carbon-Carbon Supercapacitors, J. Electrochem. Soc. 150 (2003) A292.
[53] T. Kesavan, T. Partheeban, M. Vivekanantha, M. Kundu, G. Maduraiveeran, M. Sasidharan, Hierarchical nanoporous activated carbon as potential electrode materials for high performance electrochemical supercapacitor, Microporous Mesoporous Mater. 274 (2019) 236–244.
[54] N. Sudhan, K. Subramani, M. Karnan, N. Ilayaraja, M. Sathish, Biomass-Derived Activated Porous Carbon from Rice Straw for a High-Energy Symmetric Supercapacitor in Aqueous and Non-aqueous Electrolytes, Energy Fuels. 31 (2017) 977–985.
[55] M. Karnan, K. Subramani, N. Sudhan, N. Ilayaraja, M. Sathish, *Aloe vera* Derived Activated High-Surface-Area Carbon for Flexible and High-Energy Supercapacitors, ACS Appl. Mater. Interfaces. 8 (2016) 35191–35202.

[56] D. Momodu, N.F. Sylla, B. Mutuma, A. Bello, T. Masikhwa, S. Lindberg, A. Matic, N. Manyala, Stable ionic-liquid-based symmetric supercapacitors from Capsicum seed-porous carbons, J. Electroanal. Chem. 838 (2019) 119–128.
[57] W. Chen, X. Wang, M. Feizbakhshan, C. Liu, S. Hong, P. Yang, X. Zhou, Preparation of lignin-based porous carbon with hierarchical oxygen-enriched structure for high-performance supercapacitors, J. Colloid Interface Sci. 540 (2019) 524–534.
[58] K. Subramani, N. Sudhan, M. Karnan, M. Sathish, Orange Peel Derived Activated Carbon for Fabrication of High-Energy and High-Rate Supercapacitors, ChemistrySelect. 2 (2017) 11384–11392.
[59] Z. Li, J. Liu, K. Jiang, T. Thundat, Carbonized nanocellulose sustainably boosts the performance of activated carbon in ionic liquid supercapacitors, Nano Energy. 25 (2016) 161–169.
[60] W. Sun, S.M. Lipka, C. Swartz, D. Williams, F. Yang, Hemp-derived activated carbons for supercapacitors, Carbon. 103 (2016) 181–192.
[61] S. Dai, Z. Liu, B. Zhao, J. Zeng, H. Hu, Q. Zhang, D. Chen, C. Qu, D. Dang, M. Liu, A high-performance supercapacitor electrode based on N-doped porous graphene, J. Power Sources. 387 (2018) 43–48.
[62] Y. Zhu, S. Murali, M.D. Stoller, K.J. Ganesh, W. Cai, P.J. Ferreira, A. Pirkle, R.M. Wallace, K.A. Cychosz, M. Thommes, D. Su, E.A. Stach, R.S. Ruoff, Carbon-Based Supercapacitors Produced by Activation of Graphene, Science. 332 (2011) 1537–1541.
[63] T. Kim, G. Jung, S. Yoo, K.S. Suh, R.S. Ruoff, Activated Graphene-Based Carbons as Supercapacitor Electrodes with Macro- and Mesopores, ACS Nano. 7 (2013) 6899–6905.
[64] D.T. Pham, T.H. Lee, D.H. Luong, F. Yao, A. Ghosh, V.T. Le, T.H. Kim, B. Li, J. Chang, Y.H. Lee, Carbon Nanotube-Bridged Graphene 3D Building Blocks for Ultrafast Compact Supercapacitors, ACS Nano. 9 (2015) 2018–2027.

Graphical abstract: